

## Comparative analysis of radiation-induced effects on the performance of p-type PERC and TOPCon solar cells for space applications

Fa-Jun Ma<sup>a</sup>, Guo Li<sup>a</sup>, Xutao Wang<sup>a</sup>, Haoran Wang<sup>a</sup>, Zhuangyi Zhou<sup>a</sup>, Chukwuka Uzochukwu Madumelu<sup>a</sup>, Peter Toth<sup>b</sup>, Nicholas J. Ekins-Daukes<sup>a</sup>, Gavin Conibeer<sup>a</sup>, Bram Hoex<sup>a,\*</sup>

<sup>a</sup> Australia Centre for Advanced Photovoltaics, School of Photovoltaic and Renewable Energy Engineering, University of New South Wales, Sydney, NSW, 2052, Australia  
<sup>b</sup> Extraterrestrial Power Pty Ltd.<sup>1</sup>, Sydney, NSW, Australia



### ARTICLE INFO

**Keywords:**

Silicon solar cells  
Space applications  
1 MeV electron irradiation  
Numerical simulation  
PERC  
TOPCon

### ABSTRACT

This work presents a comprehensive numerical evaluation of PERC and TOPCon technologies, focusing on the impact of radiation-induced defects. This assessment is conducted for p-type silicon solar cells as they are intrinsically more resistant to radiation defects. By rigorously calibrating recombination parameters, radiation-induced defect profiles, and other pertinent details, a robust basis is established for an in-depth comparison of the performance characteristics displayed by both architectures under space conditions. The investigation reveals that when utilizing substrates with high doping levels, both PERC and TOPCon cells exhibit nearly identical beginning-of-life (BOL) and end-of-life (EOL) performance. However, with lower substrate doping concentrations, both technologies show improved BOL efficiency. Notably, this enhanced BOL efficiency does not translate into superior EOL efficiency. This distinction in EOL efficiency can be attributed to two primary factors triggered by radiation exposure. Firstly, the emergence of defects leads to a reduction in open-circuit voltage. Secondly, dopant compensation contributes to an increase in series resistance. Specifically, for PERC cells, the challenge of elevated series resistance is further exacerbated by the requirement for majority carriers to traverse both vertically and laterally to reach the rear metal contact. When a robust defect recovery mechanism or resilient cover glass is absent, substrates characterized by lower doping levels display increased susceptibility to the adverse effects of radiation-induced defects and the subsequent dopant compensation. Under these circumstances, the TOPCon technology demonstrates a significant advantage over PERC, particularly for high electron fluence due to its full area contacts for both minority and majority charge carriers.

### 1. Introduction

Solar cells play a vital role in enabling numerous space applications, including satellites, space probes, space stations, and planetary rovers. They provide long-lasting power for scientific experiments, communication systems, propulsion, navigation, and other critical functions. Without solar cells, the feasibility and sustainability of space missions would be severely compromised. Only two photovoltaic technologies have been used beyond proof-of-principle testing for space power supply. Triple-junction InGaP/GaAs/InGaAs solar cells have been used almost exclusively for space applications for the last 20 years. Prior to that, the USA and Europe utilized silicon solar cells to power spacecraft [1–3], while the Soviet Union pursued III-V photovoltaics from the

outset [4]. The choice of solar cell technology depends on mission requirements, budget constraints, and specific performance criteria. Recently the increased popularity of short-duration space missions has led to a revival in interest in silicon based solar cells as the principal power source. This has re-opened the discussion on the relative merits at cell and array level of an inexpensive, low-efficiency technology over a more expensive, higher-efficiency technology [5]. Silicon solar cells, especially p-type silicon cells, have been extensively used in space missions for several decades and have a proven track record of success [6].

The current mainstream industrial crystalline silicon (c-Si) solar cell technology is the Passivated Emitter and Rear Cell (PERC). By inserting a dielectric layer between the substrate and the rear contact, PERC cells

\* Corresponding author.

E-mail address: [b.hoex@unsw.edu.au](mailto:b.hoex@unsw.edu.au) (B. Hoex).

<sup>1</sup> [www.extraterrestrialpower.com](http://www.extraterrestrialpower.com)

absorb more long-wavelength photons and suffer less recombination losses than the full area aluminium back surface field (BSF) solar cells that preceded them. The PERC technology has been widely adopted by manufacturers since 2017. PERC cells have undergone significant development in recent years, with a mass production average cell efficiency of 23.5 % in 2021 [7]. As the bulk lifetime of c-Si wafers has improved over time, the recombination of charge carriers at the cell surfaces and contacts has become a major obstacle to further enhancing cell efficiency. In this regard, the Tunnel Oxide Passivated Contact (TOPCon) technology has been proposed as a solution for the next-generation industrial high-efficiency silicon solar cells [8]. The TOPCon contact significantly reduces recombination losses for minority carriers while providing a low resistance for majority carriers. The TOPCon technology is also designed to be compatible with existing solar cell manufacturing lines, facilitating its rapid adoption by solar cell manufacturers.

Both commercially available p-type PERC cells and n-type TOPCon (n-TOPCon) cells are readily accessible. While cost considerations play a pivotal role, it is equally vital to determine the most optimal technology concerning both beginning-of-life (BOL) and end-of-life (EOL) performance, particularly for space applications. In pursuit of this assessment, numerical simulations were conducted utilizing real-world industrial PERC and n-TOPCon cells as the basis. The recombination parameters were carefully calibrated per the measured performance characteristics of these cells under standard test conditions. To ensure a fair and equitable comparison between the two distinct technologies, the structure of the n-TOPCon cell is systematically transformed into a p-type TOPCon (p-TOPCon) configuration, designed to possess comparable performance parameters. Afterwards an investigation into radiation-induced defects was undertaken, encompassing the replication of measured characteristics associated with p-type substrates from literature sources. Employing precisely calibrated configurations, both cell architectures undergo comprehensive examination, incorporating various doping concentrations and a range of 1 MeV electron fluences. The results presented in this work are worst-case results as they do not take any bulk defect recovery mechanism into account, so their actual performance may be significantly better.

## 2. Simulation setup

The Sentaurus TCAD software package [9] was utilized to perform comprehensive optical and electrical simulations on both the PERC and TOPCon solar cell structures. In the domain of optical simulations, the methodology involved the establishment of three-dimensional (3D) unit cells, characterized by a regular upright pyramid texture, within the simulation environment. Light trapping strategies were assessed through the implementation of the raytracing technique, encompassing considerations of both front antireflection coating (ARC) effects and rear diffuse reflection. The settings for the front ARC and rear diffuse reflection were determined by reflectivity measurements. Subsequently, the 3D distribution of absorbed photons, following calibration, was transformed into a one-dimensional (1D) optical generation profile, a format suitable for utilization in subsequent two-dimensional (2D) electrical simulations.

To ensure accurate predictions, state-of-the-art models were employed during the electrical simulation phase [10]. A summary of typical settings, encompassing the modelling of fixed charge density and intrinsic surface recombination velocity (SRV) across diverse dielectric passivation schemes, is presented in **Table 1**. Moreover, the tunnel oxide was set to 1.2 nm and the electron and hole tunnelling masses were set as  $0.42 m_0$  and  $0.33 m_0$  [11], respectively, with  $m_0$  signifying the rest mass of a free electron. The parameters governing Shockley-Read-Hall (SRH) recombination [12] were meticulously calibrated to replicate the measured characteristics of commercially available PERC and TOPCon cells under standard test conditions.

Given the level of front and rear passivation for current solar cell

**Table 1**

Typical recombination settings for dielectric passivation schemes.

Dielectric passivation	Fixed charge density [ $q/cm^2$ ]	Intrinsic surface recombination velocity for electrons and holes [ $cm/s$ ]
Hydrogenated silicon nitride ( $SiN_x:H$ )	$4 \times 10^{12}$	$1 \times 10^5, 1 \times 10^4$
Hydrogenated aluminium oxide ( $AlO_x:H/SiN_x:H$ )	$-4 \times 10^{12}$	$5 \times 10^3, 5 \times 10^2$
Tunnel silicon oxide ( $SiO_x$ )	0	$1 \times 10^3, 1 \times 10^3$

architectures, the efficiency potential for p-type solar cells is commonly constrained by the bulk minority carrier lifetime. This is particularly relevant for boron-doped substrates, where the interplay of boron and oxygen concentrations imposes an upper boundary on the minority carrier lifetime. This upper limit emerges due to the prevalence of the boron-oxygen (BO) defect complex [13], whose characteristics govern this restriction. Notably, the electron lifetime ( $\tau_{n0}$ ) was observed to exhibit an empirical dependency on boron concentration ( $N_A$ ) and oxygen interstitial concentration ( $O_i$ ), with the relationship articulated as follows:

$$\tau_{n0} = 7.675 \times 10^{39} N_A^{-0.824} O_i^{-1.748} \quad (1)$$

The capture cross section for electrons is estimated to be tenfold that of holes. Consequently, the hole lifetime ( $\tau_{p0}$ ) is ten times  $\tau_{n0}$ . The BO defects were eventually brought under control, and a viable avenue for their permanent deactivation was established via carrier injection at elevated temperatures [14]. As an alternative, the utilization of gallium (Ga) doping for p-type substrates emerged as a viable strategy to circumvent BO defects [15]. In the absence of BO defects, the maximum achievable lifetimes were found to be mainly dependent on the substrate's doping concentration [16]. Under the circumstance where the excess carrier density ( $\Delta n$ ) equals 10 % of the hole concentration ( $p_0$ ), the bulk lifetime ( $\tau_b$ ) within a p-type substrate can be described through the following empirical parameterization [16]:

$$\frac{1}{\tau_b} = \frac{1}{5500 \mu s} + \frac{p_0^2}{5 \times 10^{35} cm^{-6} \mu s} \quad (2)$$

The bulk lifetime depends on the interplay of SRH, Auger, and radiative recombination mechanisms within the substrate. Following the successful permanent deactivation of BO defects, the manifestation of SRH recombination can be effectively captured through the modelling of a mid-bandgap defect, characterized by an electron-to-hole capture cross-section ratio of 12. This relationship implies that  $\tau_{p0}$  is twelve times higher than  $\tau_{n0}$ . The representation of the SRH lifetime ( $\tau_{SRH}$ ) can be simplified, as described in Ref. [17], in the following manner:

$$\tau_{SRH} = \tau_{n0} + \frac{\tau_{p0} \Delta n}{\Delta n + N_A} \quad (3)$$

At an injection level of 10 % of the hole concentration, Equation (3) can be further simplified to

$$\tau_{SRH} = \frac{23 \tau_{p0}}{132} \quad (4)$$

From the relationship between  $\tau_{SRH}$  and  $\tau_b$ , the hole lifetime can be determined as

$$\frac{1}{\tau_{p0}} = \frac{23}{132 \tau_{SRH}} = \frac{23}{132} \left( \frac{1}{\tau_b} - \frac{1}{\tau_{Aug}} - \frac{1}{\tau_{Rad}} \right) \quad (5)$$

where the Auger lifetime ( $\tau_{Aug}$ ) can be evaluated employing the Richter parameterization [18], whereas the radiative lifetime ( $\tau_{Rad}$ ) is interconnected with the radiative recombination coefficient of  $4.73 \times 10^{-15} cm^3/s$ . **Table 2** provides a comprehensive compilation of the parameters for varying boron concentrations ranging from  $10^{14}$  to  $10^{16} cm^{-3}$ , after the achievement of permanent BO recovery at a temperature of 25 °C. In

**Table 2**

The electron and hole lifetimes in p-type c-Si after permanent BO recovery at 25 °C.

$N_A$ cm <sup>-3</sup>	$n_0$ cm <sup>-3</sup>	$p_0$ cm <sup>-3</sup>	$\Delta n$ cm <sup>-3</sup>	$n_{i,eff}$ cm <sup>-3</sup>	$\tau_{Aug}$ s	$\tau_{Rad}$ s	$\tau_b$ s	$\tau_{po}$ s
$1 \times 10^{14}$	$6.95 \times 10^5$	$1 \times 10^{14}$	$1 \times 10^{13}$	$8.34 \times 10^9$	876.68	21.14	$5.50 \times 10^{-3}$	$3.16 \times 10^{-2}$
$5 \times 10^{14}$	$1.42 \times 10^5$	$5 \times 10^{14}$	$5 \times 10^{13}$	$8.43 \times 10^9$	38.94	4.23	$5.48 \times 10^{-3}$	$3.15 \times 10^{-2}$
$1 \times 10^{15}$	$7.22 \times 10^4$	$9.99 \times 10^{14}$	$9.99 \times 10^{13}$	$8.51 \times 10^9$	10.19	2.12	$5.44 \times 10^{-3}$	$3.13 \times 10^{-2}$
$5 \times 10^{15}$	$1.54 \times 10^4$	$4.98 \times 10^{15}$	$4.98 \times 10^{14}$	$8.81 \times 10^9$	0.46	0.42	$4.32 \times 10^{-3}$	$2.53 \times 10^{-2}$
$1 \times 10^{16}$	$8.13 \times 10^3$	$9.93 \times 10^{15}$	$9.93 \times 10^{14}$	$9.03 \times 10^9$	0.12	0.21	$2.64 \times 10^{-3}$	$1.57 \times 10^{-2}$
$1.52 \times 10^{16}$	$5.58 \times 10^3$	$1.5 \times 10^{16}$	$1.5 \times 10^{15}$	$9.20 \times 10^9$	0.054	0.14	$1.58 \times 10^{-3}$	$9.47 \times 10^{-3}$

this context,  $n_{i,eff}$  denotes the effective intrinsic carrier density, a value deduced utilizing the Schenk bandgap narrowing model [19] while considering a condition of low injection.

Solar cells deployed in low Earth orbit (LEO) are exposed to an array of environmental factors. Among these, a prominent factor is the continuous barrage of high-energy particles, primarily encompassing electrons ranging from 40 keV to 7 MeV and protons spanning from 100 keV to 400 MeV [20]. The slowing of these particles within the active semiconductor creates displacement damage and hence the generation of point defects. This computational study considers the detrimental consequences of high-energy particle irradiation on p-type silicon solar cells. 1 MeV electron irradiation was considered since damage is relatively uniform throughout the thickness of the solar cell device and it is also one of the standard energies for which detailed characterization are performed. Particularly, defects under 1 MeV electron irradiation were characterized by Yamaguchi et al. through deep-level transient spectroscopy (DLTS) measurements [21], revealing the presence of two donor defects and three acceptor defects. The energy levels and capture cross-sections associated with these defects were directly adopted within simulations as listed in Table 3.

Additionally, the introduction rate of each defect was rigorously calibrated by modelling a 50 μm space cell [3]. A simplified modelling approach for the back-surface field and reflector (BSFR) structure was adopted as described in Ref. [22]. The specification of introduction rates and defect profiles was achieved through the process of reproducing spectral response and short-circuit current density  $J_{sc}$ , as a function of electron fluence.

### 3. Results and discussion

#### 3.1. Modelling PERC solar cells

A comprehensive suite of characterization techniques, encompassing reflectivity (R), external quantum efficiency (EQE), and light current density voltage (LJV) measurements, was conducted across a dataset comprising over 20 M4 size PERC solar cells, featuring five busbars and 106 front fingers. The results from a representative PERC cell were employed for subsequent modelling. Due to the inherent symmetry of solar cell structures, the optical simulation unit cell was reduced to a 3D domain, encompassing just one-quarter of a pyramid. Furthermore, for electrical simulations, the unit cell was further simplified into a 2D domain, as depicted in Fig. 1(a). The optical simulation phase was initiated with the aim of accurately replicating the reflectivity curve, thereby facilitating the determination of photon absorption within the

solar cell. Through in-depth analysis of reflectivity data spanning the range of 400–1000 nm, the ARC layer, comprised of hydrogenated silicon nitride ( $\text{SiN}_x\text{:H}$ ), was found to have an optimal thickness of 80 nm with a refractive index of 1.99 at a wavelength of 600 nm. Furthermore, by leveraging reflectivity data from 1000 to 1200 nm, the diffuse reflection emanating from the rear surface was effectively characterized using a Phong factor of 50 and an associated broadband reflectivity of 96 %, which is consistent with reference [23].

Electrical simulations were systematically conducted to replicate the EQE and LJV curves of the measured solar cell, utilizing the photo-generation profile derived from the earlier optical simulations. The substrate's resistivity was determined to be approximately 1 Ωcm. In alignment with the parameters established in Ref. [24], the profiles for the front emitter and the rear local BSF were conservatively set at 107 Ω/sq and 10 Ω/sq, respectively. Detailed specifications for the dielectric passivation on both the front and rear sides can be referenced from Table 1. From the EQE data presented in Fig. 1(b)—a front-side metal fraction of 3.79 % was established, which in turn accurately reproduced the measured  $J_{sc}$ . In the pursuit of replicating the measured open-circuit voltage  $V_{oc}$ , it became evident that a hole lifetime of 1.86 ms for the substrate was required, a value notably lower than the 9.51 ms calculated in Table 2 after complete BO deactivation, likely resulting from residual SRH bulk defects.

#### 3.2. Modelling TOPCon solar cells

Similarly, the method employed in the preceding analysis was extended to a representative n-TOPCon solar cell. In this context, 3D optical simulations were conducted, considering a front structure characterized by a regular upright pyramidal configuration and a rear surface modelled using a Phong factor of 15 coupled with a broadband reflectivity of 88 %. Within the ARC stack, the optimal thickness for  $\text{SiN}_x\text{:H}$  was determined to be 80 nm, with a refractive index of 1.96 at a wavelength of 600 nm in combination with a hydrogenated aluminium oxide ( $\text{AlO}_x\text{:H}$ ) with a thickness of 10 nm, as determined through a detailed analysis of reflectivity data spanning the range of 400–1000 nm as shown in Fig. 2(b). For the subsequent electrical simulations, a 2D unit cell, depicted in Fig. 2(a), was employed. The n-type substrate was found to have a resistivity of approximating 1.3 Ωcm. The front boron emitter profile was set at 88 Ω/sq. The experimental phosphorus diffusion profile within the n<sup>+</sup> poly region was characterized using the electrochemical capacitance-voltage (ECV) technique and the thickness was found to be 220 nm. By effectively reproducing the EQE results as depicted in Fig. 2(b), alongside the corresponding LJV curves, the appropriate front metal fraction was determined to be 3.4 %. Furthermore, to replicate the measured  $V_{oc}$ , a hole carrier lifetime of 2.23 ms was found for the substrate.

P-type silicon solar cells have demonstrated enhanced resilience to radiation when compared to those fabricated on n-type substrates [2] and this explains their dominance in early space missions as well as for terrestrial solar cells. In order to establish an equitable comparison against the PERC structure, the configuration of the n-TOPCon cell shown in Fig. 2(a) underwent slight modifications to transform it into a TOPCon configuration on a p-type substrate, as depicted in Fig. 3(a). On

**Table 3**

Defect characteristics from DLTS characterizations [21].

Defect type	Reference energy level	Energy [eV]	Capture cross section [cm <sup>2</sup> ]
Donor	Conduction band	-0.18	$1.8 \times 10^{-16}$
Donor	Conduction band	-0.71	$3.55 \times 10^{-13}$
Acceptor	Valence band	+0.18	$8.9 \times 10^{-17}$
Acceptor	Valence band	+0.36	$7.2 \times 10^{-16}$
Acceptor	Valence band	+0.56	$6.3 \times 10^{-13}$

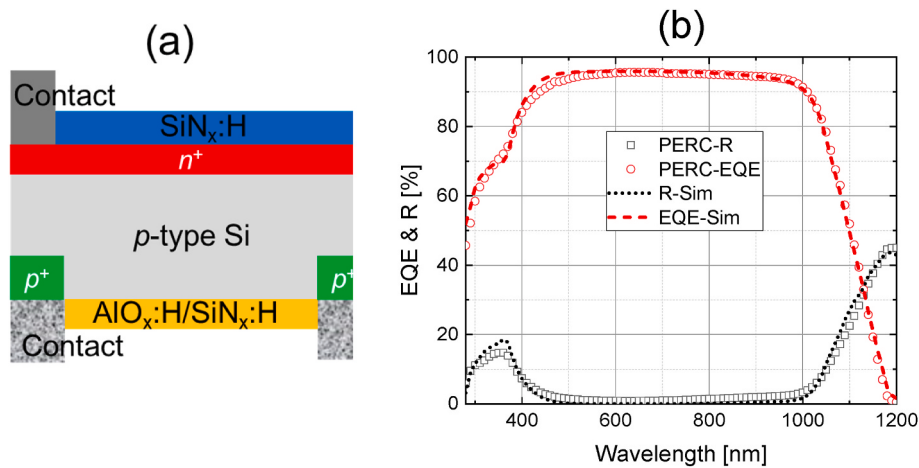


Fig. 1. (A) sketch of 2D unit cell of the PERC cell and (b) reasonable agreements between measured EQE and R curves and simulated results.

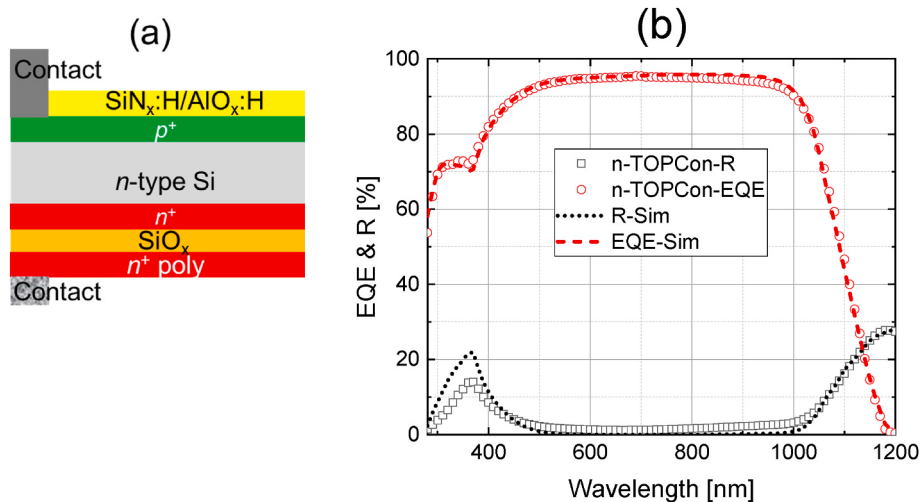


Fig. 2. (A) sketch of 2D unit cell of the n-TOPCon cell and (b) reasonable agreements between measured EQE and R curves and simulated results.

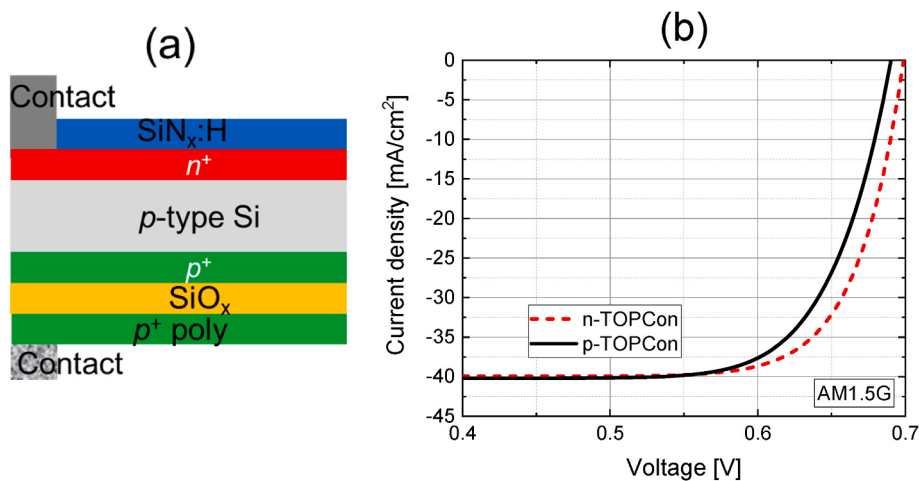


Fig. 3. (A) sketch of 2D unit cell of the p-TOPCon cell and (b) light JV of n-TOPCon and p-TOPCon.

the front side, both the emitter and the ARC were kept consistent with the PERC configuration in Fig. 1(a). The metal fraction remained constant at 3.4 %. Parameters such as substrate resistivity and SRH lifetimes were aligned with the values for PERC. On the rear side, the boron

concentration within the p<sup>+</sup> poly region was set to  $6 \times 10^{19} \text{ cm}^{-3}$  and the in-diffusion profile followed a Gaussian distribution as in Ref. [25]. The resulting sheet resistance was 76 Ω/sq, the same as phosphorus doped poly. Subsequent electrical simulations were carried out

following these adaptations, revealing that the p-TOPCon performance exhibited similarity to its n-TOPCon counterpart, as indicated by the LJV outcomes illustrated in Fig. 3(b). The observed 8 mV reduction in  $V_{oc}$  was attributed to a substantially lower minority carrier lifetime in p-type vs n-type silicon. The measured and simulated figure of merits are listed in Table 4 for both PERC and TOPCon cells.

### 3.3. Higher bulk lifetime

Both the PERC as well as the TOPCon structures hold the potential for high efficiencies. As deduced from the preceding two sections, the prevailing loss mechanism in both cell types stems from SRH recombination in the bulk. Subsequent elimination of BO defects led to a quintupling of the electron lifetime, a value that can be further increased by increasing the substrate resistivity, as outlined in Table 2. Advances in technology have ushered in cost-effective Ga-doped substrates devoid of the BO defect. It may be reasonably assumed that Ga-doped substrates boast identical bulk lifetimes to their B-doped counterparts, post-permanent BO deactivation.

Higher substrate lifetimes facilitate superior performance at BOL conditions. Concurrently, intrinsic recombination losses diminish as substrate resistivity decreases, leading to higher efficiencies. However, it's imperative to optimize the finger pitch to keep the series resistance sufficiently low. To conveniently gauge the influence of enhanced SRH lifetimes coupled with lower doping concentrations across both architectures, Suns- $V_{oc}$  simulations were undertaken, thereby mitigating the influence of series resistance. As evident from Fig. 4, initial limitations in both PERC and p-TOPCon cells stemmed from BO defects, suggesting the potential for efficiency enhancements through improved bulk minority carrier lifetimes. With an electron lifetime increased by fivefold post BO deactivation, the pseudo efficiency increased by 0.7 % absolute for both PERC and p-TOPCon. This incremental trend persisted for  $J_{sc}$ ,  $V_{oc}$  and FF as substrate resistivity increased, aligning with expectations. At a doping concentration of  $10^{14} \text{ cm}^{-3}$ , a pseudo efficiency increase of 1 % absolute was observed for both PERC and p-TOPCon configurations.

### 3.4. Radiation-induced defects

Solar cells deployed in space are subject to degradation induced by high energy particles from the solar wind, comprising primarily protons and electrons of varying energy levels. The displacement damage dose (DDD) methodology, pioneered by the U.S. Naval Research Laboratory (NRL) [26], is well suited to the analysis of silicon solar cells since the Non-Ionizing Energy Loss (NIEL) for silicon is well known, allowing the full radiation response of a solar cell to be determined for both protons and electrons to be made from measurements of one proton energy and two electron energies [27]. Assumptions regarding uniform defects triggered by 1 MeV electrons, and the identification of five such defects has been derived from DLTS measurements [21].

Building upon the simulation methodology applied to the PERC and n-TOPCon architectures, a 2D unit cell configuration representative of the 50  $\mu\text{m}$  back surface field region (BSFR) space cell [28], illustrated in Fig. 5(a), was established within the simulation environment. Following the simulation approach by Hamache et al. [22], the current study also embraced a simplified approach. On the front side, the emitter was

characterized by a constant doping concentration of  $10^{19} \text{ cm}^{-3}$ , accompanied by a junction depth of 150 nm. The rear BSF layer maintains a constant doping level of  $5 \times 10^{18} \text{ cm}^{-3}$ , with a junction depth extending to 550 nm. The substrate, doped with boron, exhibited a concentration of  $10^{15} \text{ cm}^{-3}$ . A substrate lifetime of 30  $\mu\text{s}$  was stipulated as reference [22]. The dielectric passivated front side was modelled incorporating a SRV of 10,000 cm/s, complemented by a zero fixed charge density.

The solar cell in question exhibits exceptional internal quantum efficiency, surpassing 95 %. Analysis of the BOL EQE, as displayed in Fig. 5(b) [3], indicates that the optical characteristics of the cell are instrumental in reproducing the EQE profile. However, detailed insights into the light management strategy for this particular cell are somewhat limited. An exploration of the  $\text{TiO}_2/\text{Al}_2\text{O}_3$  ARC stack through optical simulations suggests that the front side of the cell was not planar; otherwise, achieving a  $J_{sc}$  of 40 mA/cm<sup>2</sup> would be unattainable. Yet, it is very likely that the front surface was partially planar and partially textured with inverted pyramidal structures as indicated in Ref. [29]. From a design standpoint for space applications, adopting a fully textured front surface may lead to higher in-orbit operating temperatures, potentially counteracting the optical benefits derived from light trapping. This presents a supplementary uncertainty concerning the texture ratio. The distinctive concave trend observed in the EQE data between 400 and 800 nm is likely linked to the ARC stack. A decline in EQE response beyond 800 nm suggests limited photon absorption (associated with high photon rejection) for longer wavelengths. This behaviour aligns with the design of BSFR, which effectively reflects longer-wavelength photons back into space.

The absence of critical information about the light trapping strategy hampers the ability to achieve a precise alignment with the BOL EQE. Additionally, the shape of the BOL EQE influences the EQE profile following an electron fluence of  $4 \times 10^{16} \text{ cm}^{-2}$ . By fine-tuning the introduction rates of the five identified defects, it was established that the introduction rate of the donor defect positioned 0.18 eV below the conduction band ( $E_c$ ) needed to be an order of magnitude higher than that of the acceptor defect located 0.18 eV above the valence band ( $E_v$ ). Furthermore, it became evident that there was no constant introduction rate capable of yielding consistent agreement across all EQE curves for varying electron fluences. Usually, the defect generation profile is assumed to be uniform in the substrate after electron irradiation. However, it was found that a uniform defect generation profile failed to yield satisfactory alignment with EQE values between 800 and 1000 nm for the solar cell that was exposed to a 1 MeV electron fluence of  $5 \times 10^{16} \text{ cm}^{-2}$ .

This discrepancy implies that fewer defects were generated on the rear side, which is justified as electrons gradually lose their energy in the substrate. A plausible supposition is that defect generation followed an exponential decay from the front to the rear side. With this assumption, favourable concordance with all EQE results was achieved, as depicted in Fig. 6(a). The depth factor characterizing the exponential function was estimated to be approximately 960  $\mu\text{m}$ . Given this relatively large depth factor, the defect density at a depth of 50  $\mu\text{m}$  is only 5 % lower than that at the front surface. This finding aligns with the conventional assumption of a uniform defect distribution throughout the substrate. It is important to note that consistent introduction rates capable of reconciling all EQE curves for different electron fluences remained elusive, hinting at significant sample-to-sample variations. By manipulating the front metal fraction, the simulated cell achieved the same  $J_{sc}$  of 40 mA/cm<sup>2</sup>,  $V_{oc}$  of 605 mV, fill factor (FF) of 78, efficiency of 14 % under 25 °C and AM0 conditions. Through careful adjustments of the introduction rates, the observed abnormal  $J_{sc}$  behaviour was successfully reproduced, as illustrated in Fig. 6(b).

Table 5 lists the carrier capture cross section values ( $\sigma$ ) and introduction rates ( $\eta$ ) from previous publications together with the values used in this work. These values have discrepancies even from the same authors. Yamaguchi et al. performed calculations to reproduce the  $J_{sc}$

**Table 4**  
Measured and simulated one-sun I-V parameters of PERC and TOPCon cells.

Parameters	PERC exp	n-TOPCon exp	PERC sim	n-TOPCon sim	p-TOPCon sim
$J_{sc}$ [mA/ $\text{cm}^2$ ]	40.43	39.95	40.43	39.95	40.21
$V_{oc}$ [mV]	688.5	698.8	688.5	698.8	690.2
Eff [%]	22.85	23.14	22.91	23.28	22.73
FF [%]	82.09	82.89	82.10	83.20	81.69

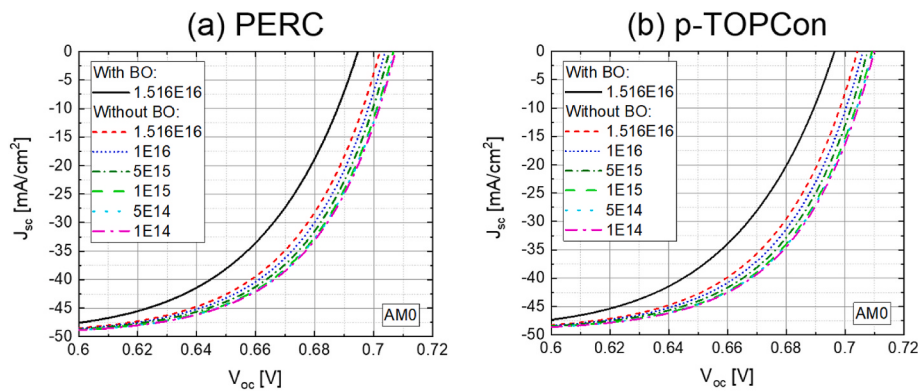


**Fig. 4.** Suns- $V_{oc}$  results from substrates before and after BO recovery, and substrates with lower doping concentrations using (a) PERC and (b) p-TOPCon technologies.

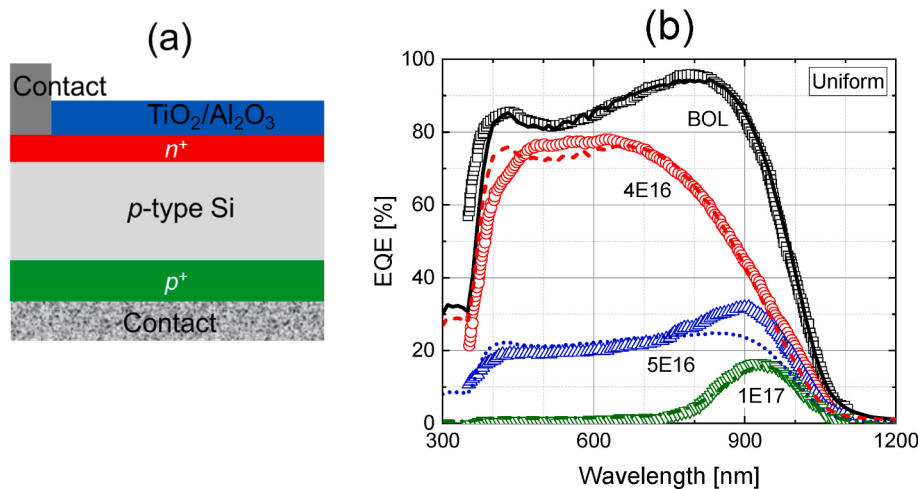


**Fig. 5.** (A) 2D unit cell of the 50  $\mu\text{m}$  BSFR space cell and (b) measured EQE vs. simulated results based on the uniform defect generation assumption.

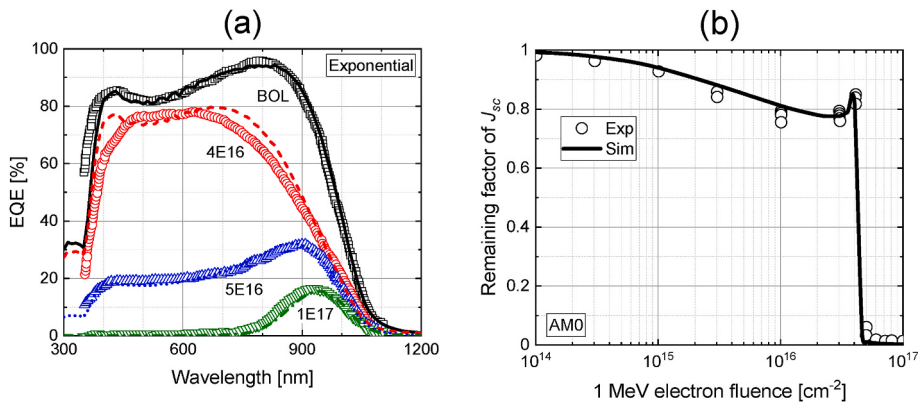


**Fig. 6.** Assuming an exponential defect generation profile with a depth factor of 960  $\mu\text{m}$ , reasonable agreements can be obtained for (a) EQE and (b) abnormal  $J_{sc}$  behaviour.

degradation behaviour as well as EQE curves [3]. However, they did not reveal their approach and the relevant details. Hamache et al. simulated the  $J_{sc}$  degradation with all the traps and found it was necessary to increase the uniform introduction rate of the donor trap (-0.20) to 0.04 cm<sup>-1</sup> [22]. Neither did they reproduce EQE curves, nor did they adjust introduction rates of the rest traps to fit the  $J_{sc}$  degradation data. In this work, capture cross section values from DLTS measurements [21] were adopted while all introduction rates were treated as fitting variables. As

explained earlier, it was necessary to assume a nonuniform introduction of traps, which was modelled using an exponential decay function with a depth factor of 960  $\mu\text{m}$  and the introduction rates in Table 5 were calculated from the front surface. The introduction rates of deep traps (+0.56, -0.71) were reduced considerably as they have high effects on SRH recombination.

**Table 5**

Capture cross section values and introduction rates from previous publications together with this work.

Trap energy levels	Uniform introduction [21]		Uniform introduction [3]		Uniform introduction [22]		Nonuniform introduction (this work)	
	$\sigma$ [cm $^{-2}$ ]	$\eta$ [cm $^{-1}$ ]	$\sigma$ [cm $^{-2}$ ]	$\eta$ [cm $^{-1}$ ]	$\sigma$ [cm $^{-2}$ ]	$\eta$ [cm $^{-1}$ ]	$\sigma$ [cm $^{-2}$ ]	$\eta$ [cm $^{-1}$ ]
+0.18	$8.9 \times 10^{-17}$	$3 \times 10^{-3}$	$3.1 \times 10^{-15}$	$2 \times 10^{-3}$	$3.1 \times 10^{-15}$	$2 \times 10^{-3}$	$8.9 \times 10^{-17}$	$3.1 \times 10^{-3}$
+0.36	$7.2 \times 10^{-16}$	$7 \times 10^{-3}$	$6.2 \times 10^{-15}$	$1.6 \times 10^{-2}$	$6.2 \times 10^{-15}$	$1.6 \times 10^{-2}$	$7.2 \times 10^{-16}$	$7.2 \times 10^{-3}$
+0.56	/	/	$6.3 \times 10^{-13}$	$2 \times 10^{-3}$	$6.3 \times 10^{-13}$	$2 \times 10^{-3}$	$6.3 \times 10^{-13}$	$1.0 \times 10^{-4}$
-0.71	/	/	$3.55 \times 10^{-13}$	$4 \times 10^{-3}$	$3.55 \times 10^{-13}$	$4 \times 10^{-3}$	$3.55 \times 10^{-13}$	$2.1 \times 10^{-4}$
-0.20 (-0.18)	$1.8 \times 10^{-16}$	$1.3 \times 10^{-2}$	$9.9 \times 10^{-15}$	$2 \times 10^{-3}$	$9.9 \times 10^{-15}$	$4 \times 10^{-2}$	$1.8 \times 10^{-16}$	$3.0 \times 10^{-2}$

### 3.5. PERC vs p-TOPCon

The initial efficiencies at BOL for both the PERC and p-TOPCon configurations, as measured under AM0 conditions, stood at 21.18 % and 21.07 % respectively. It is noteworthy that these two cells displayed comparable temperature coefficients, namely 0.349 %/°C for PERC and 0.344 %/°C for p-TOPCon. The investigation into the impact of space irradiation encompassed the incorporation of five exponential decay defect profiles, as shown in Section D, into the substrate. This integration maintained the original SRH lifetimes without BO defects. The introduction rates for these five defects were kept constant, ensuring a linear scaling of defect densities with electron fluence. The resultant performance characteristics, following exposure to various fluence levels during 1 MeV electron irradiation, were normalized with respect to their BOL counterparts. Illustrated in Fig. 7, a gradual degradation in all performance characteristics was observed with increasing electron fluence. Notably, deviations from expected behaviour in  $J_{sc}$  were absent due to the substantial substrate doping levels. As discussed in Section D, a fluence exceeding  $10^{17}$  cm $^{-2}$  was required to induce significant majority carrier removal and even substrate inversion. Within the investigated fluence range, both cell configurations demonstrated nearly identical patterns of performance degradation.

As explained in Section C, both TOPCon and PERC can enhance their BOL performance by adopting lowly doped substrates with optimized pitch. It is of notable interest to investigate whether the utilization of lightly doped substrates could also translate into improved EOL performance. To this end, the acceptor concentration within the substrate was varied from  $10^{14}$  to  $10^{16}$  cm $^{-3}$  for both configurations. Three discrete electron fluence levels, namely  $1 \times 10^{14}$ ,  $5 \times 10^{14}$  and  $1 \times 10^{15}$  cm $^{-2}$ , were examined. Within an LEO environment, these fluence values correspond approximately to anticipated operational periods of around one, five, and ten years, respectively. As depicted in Fig. 8, the EOL efficiency of both cell types exhibited a marked reduction with decreasing substrate acceptor doping levels, with the effect being more pronounced in the case of the PERC architecture. Notably, the variation in EOL  $J_{sc}$ , although not shown, exhibited marginal increments with increasing substrate resistivity, thereby discounting its contribution to

the observed EOL efficiency trends. The pivotal factors responsible for the observed EOL efficiency behaviour were narrowed down to the EOL  $V_{oc}$  and FF.

Evidently, the  $V_{oc}$  response of the PERC cell shown in Fig. 9(a) exhibited similarity to that of the p-TOPCon cell depicted in Fig. 9(b) concerning the effects of substrate doping and electron fluence. However, the PERC cell displayed a more pronounced decline in FF compared to the p-TOPCon cell for lightly doped substrates. These behaviours can be attributed to the creation of SRH defects and the removal of majority carriers, as discussed in Section D. The former primarily governs variations in  $V_{oc}$ , while the latter predominantly influences FF behaviour. A higher electron fluence resulted in a higher radiation-induced defect density, which explains the  $V_{oc}$  difference between electron fluences at the same acceptor concentration. With a decrease in substrate doping level, there was an observable rise in the minority carrier concentration, leading to an increased SRH recombination due to radiation-induced defects, despite identical defect profiles (e.g.  $1 \times 10^{14}$  cm $^{-2}$ ) at each acceptor concentration, thereby yielding a comparable  $V_{oc}$  response. The dopant compensation (majority carrier removal) is directly proportional to the magnitude of electron fluence. Consequently, substrate resistivity changed as a function of electron fluence with a relatively higher impact for lightly doped substrates. In comparison to the p-TOPCon configuration, the PERC cell has a higher series resistance, as the majority carriers must diffuse laterally to the localized contacts according to Fig. 1(a).

### 4. Summary

For the context of space applications, a comprehensive numerical evaluation is undertaken to assess the viability of both c-Si PERC and TOPCon solar cell technologies. Commencing with industrial PERC and n-TOPCon cells, meticulous calibration procedures are implemented, primarily concerning recombination parameters, by aligning them with the experimentally determined QE and I-V characteristics under standard test conditions. Next, the parameters derived for the n-type TOPCon cell were used to simulate a p-type TOPCon cell as it is well known that p-type silicon is less sensitive to radiation damage compared to n-

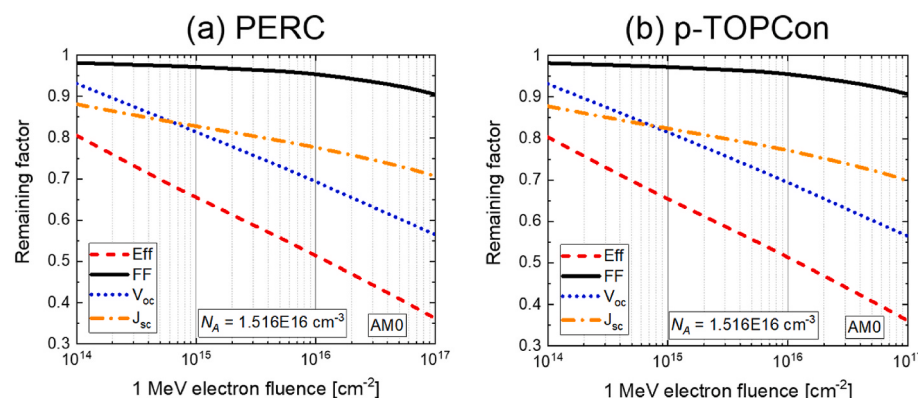


**Fig. 7.** Normalized performance characteristics as a function of 1 MeV electron fluence, of (a) PERC and (b) p-TOPCon. The values were normalized to the BOL performance.

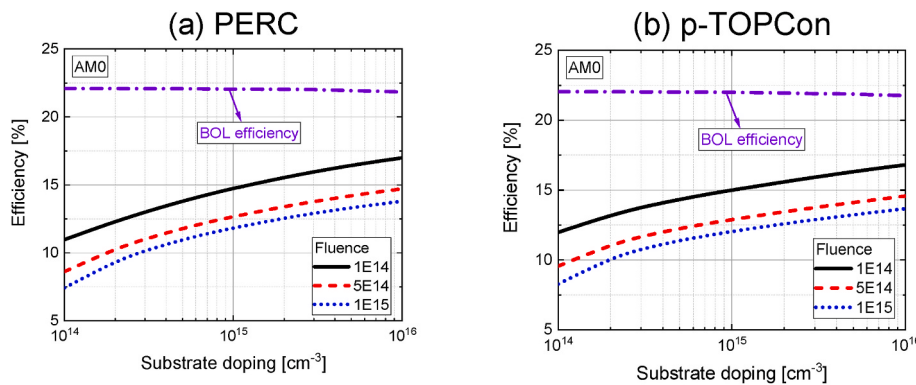


**Fig. 8.** The EOL efficiencies of (a) PERC and (b) p-TOPCon as a function of the substrate acceptor concentration ranging from  $10^{14}$  to  $10^{16}$  cm<sup>-3</sup> for three electron fluences,  $1 \times 10^{14}$ ,  $5 \times 10^{14}$  and  $1 \times 10^{15}$  cm<sup>-2</sup>, respectively.

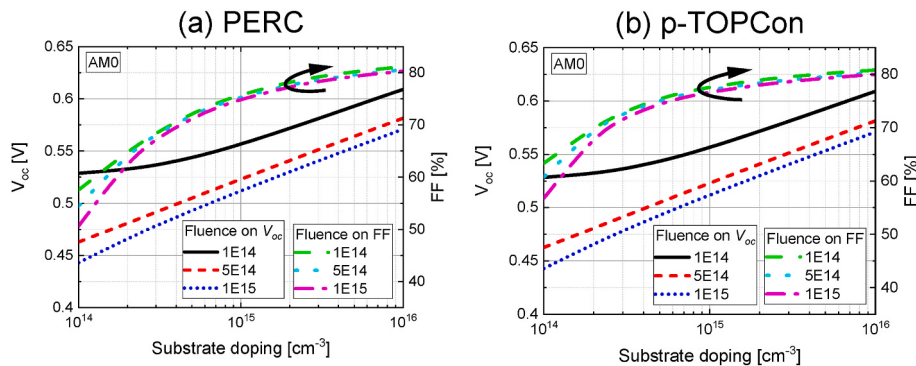


**Fig. 9.** The EOL  $V_{oc}$  and FF of (a) PERC and (b) p-TOPCon on substrates with the acceptor concentration spanning from  $10^{14}$  to  $10^{16}$  cm<sup>-3</sup> for three electron fluences,  $1 \times 10^{14}$ ,  $5 \times 10^{14}$  and  $1 \times 10^{15}$  cm<sup>-2</sup>, respectively.

type silicon. The p-type silicon bulk is simulated assuming no recombination due to boron-oxygen complex by using gallium as the dopant. The effects of electron irradiance on solar cell performance are deduced from replicating literature values reported for a 50 μm BSFR cell [3], leading to the derivation of defect profiles and introduction rates pertaining to radiation-induced defects. Specifically, the defect generation profile was identified to conform to an exponential decay pattern, characterized by a relatively high depth factor of 960 μm. Next, these defects are introduced in the p-type PERC and TOPCon solar cells and their performance is modelled for wide range of acceptor densities and electron fluences.

Across a substrate doping range spanning from  $10^{14}$  to  $10^{16}$  cm<sup>-3</sup>, both PERC and p-TOPCon cells exhibited improved BOL power conversion efficiency with substrate resistivity. However, this enhanced BOL efficiency did not necessarily translate into superior EOL efficiency. This performance gap could be attributed to two predominant effects stemming from electron irradiation: the formation of SRH defects, leading to a reduction in  $V_{oc}$ , and the removal of majority carriers, resulting in an increase of series resistance. Specifically, for PERC cells, the challenge of increased series resistance was accentuated by the requirement for majority carriers to traverse not only vertically but also laterally to reach the bottom metal contact. In scenarios where an effective defect recovery mechanism or a robust cover glass is lacking, substrates characterized by low doping levels proved to be more susceptible to the detrimental influences of radiation-induced defects and the ensuing majority carrier removal. Within this context, TOPCon technology shows a slight advantage over PERC due to its full area contact for both minority and majority carriers. For substrates characterized by high doping concentrations, the EOL performance of both cell types was quite similar.

## CRediT authorship contribution statement

**Fa-Jun Ma:** Writing – review & editing, Writing – original draft, Visualization, Validation, Software, Methodology, Investigation, Formal analysis, Data curation, Conceptualization. **Guo Li:** Writing – review & editing, Resources, Data curation. **Xutao Wang:** Writing – review & editing. **Haoran Wang:** Writing – review & editing. **Zhuangyi Zhou:** Writing – review & editing. **Chukwuka Uzochukwu Madumelu:** Writing – review & editing. **Peter Toth:** Writing – review & editing, Supervision, Project administration, Funding acquisition, Conceptualization. **Nicholas J. Ekins-Daukes:** Writing – review & editing, Resources, Funding acquisition. **Gavin Conibeer:** Writing – review & editing, Supervision, Project administration, Funding acquisition. **Bram Hoex:** Writing – review & editing, Visualization, Supervision, Project administration, Funding acquisition, Conceptualization.

## Declaration of competing interest

The authors declare that they have no known competing financial interests or personal relationships that could have appeared to influence the work reported in this paper.

## Data availability

Data will be made available on request.

## Acknowledgements

This work was financially supported by the Australian Research Council under the grant LP210200883. During the preparation of the original draft, F.-J. Ma used GPT-3.5 to improve readability and English.

After using this tool, the authors reviewed and edited the content as needed and take full responsibility for the content of the publication. All simulations were performed on the Katana high-performance computing cluster (doi:10.26190/669x-a286).

## References

- [1] S.G. Bailey, R. Raffaele, K. Emery, Space and terrestrial photovoltaics: Synergy and diversity, *Prog. Photovoltaics Res. Appl.* 10 (6) (Sep. 2002) 399–406, <https://doi.org/10.1002/pip.446>.
- [2] P.A. Iles, *Evolution of Space Solar Cells*, 2001.
- [3] M. Yamaguchi, Radiation-resistant solar cells for space use, *Sol. Energy Mater. Sol. Cell.* 68 (1) (Apr. 2001) 31–53, [https://doi.org/10.1016/S0927-0248\(00\)00344-5](https://doi.org/10.1016/S0927-0248(00)00344-5).
- [4] V.M. Andreev, GaAs and high-efficiency space cells, in: *Practical Handbook of Photovoltaics*, Elsevier, 2012, pp. 399–416, <https://doi.org/10.1016/B978-0-12-385934-1.00012-X>.
- [5] N.S. Fatemi, H.E. Pollard, H.Q. Hou, P.R. Sharps, Solar array trades between very high-efficiency multi-junction and Si space solar cells, in: *Conference Record of the Twenty-Eighth IEEE Photovoltaic Specialists Conference*, IEEE, 2000, pp. 1083–1086, <https://doi.org/10.1109/PVSC.2000.916075>.
- [6] M. Yamaguchi, K. Lee, K. Araki, N. Kojima, Y. Okuno, M. Imaizumi, Analysis for nonradiative recombination loss and radiation degradation of Si space solar cells, *Prog. Photovoltaics Res. Appl.* 29 (1) (Jan. 2021) 98–108, <https://doi.org/10.1002/pip.3346>.
- [7] M.A. Green, E.D. Dunlop, J. Hohl-Ebinger, M. Yoshita, N. Kopidakis, X. Hao, Solar cell efficiency tables (Version 58), *Prog. Photovoltaics Res. Appl.* 29 (7) (Jul. 2021) 657–667, <https://doi.org/10.1002/pip.3444>.
- [8] J. Schmidt, R. Peibst, R. Brendel, Surface passivation of crystalline silicon solar cells: Present and future, *Sol. Energy Mater. Sol. Cell.* 187 (Dec. 2018) 39–54, <https://doi.org/10.1016/j.solmat.2018.06.047>.
- [9] “Sentaurus TCAD.” Synopsys Inc., Sunnyvale, CA [Online]. Available, <https://www.synopsys.com/manufacturing/tcad.html>, 2023. (Accessed 10 September 2023).
- [10] P.P. Altermatt, Models for numerical device simulations of crystalline silicon solar cells—a review, *J. Comput. Electron.* 10 (3) (Sep. 2011) 314–330, <https://doi.org/10.1007/s10825-011-0367-6>.
- [11] H. Steinkemper, F. Feldmann, M. Bivour, M. Hermle, Numerical simulation of carrier-selective electron contacts featuring tunnel oxides, *IEEE J. Photovoltaics* 5 (5) (Sep. 2015) 1348–1356, <https://doi.org/10.1109/JPHOTOV.2015.2455346>.
- [12] W. Shockley, W.T. Read, Statistics of the recombinations of holes and electrons, *Phys. Rev.* 87 (5) (Sep. 1952) 835–842, <https://doi.org/10.1103/PhysRev.87.835>.
- [13] K. Bothe, R. Sinton, J. Schmidt, Fundamental boron-oxygen-related carrier lifetime limit in mono- and multicrystalline silicon, *Prog. Photovoltaics Res. Appl.* 13 (4) (Jun. 2005) 287–296, <https://doi.org/10.1002/pip.586>.
- [14] S.W. Glunz, S. Rein, J.Y. Lee, W. Warta, Minority carrier lifetime degradation in boron-doped Czochralski silicon, *J. Appl. Phys.* 90 (5) (Sep. 2001) 2397–2404, <https://doi.org/10.1063/1.1389076>.
- [15] S.W. Glunz, S. Rein, J. Knobloch, W. Wetting, T. Abe, Comparison of boron- and gallium-doped p-type Czochralski silicon for photovoltaic application, *Prog. Photovoltaics Res. Appl.* 7 (6) (Nov. 1999) 463–469, [https://doi.org/10.1002/\(SICI\)1099-159X\(199911/12\)7:6<463::AID-PIP293>3.0.CO;2-H](https://doi.org/10.1002/(SICI)1099-159X(199911/12)7:6<463::AID-PIP293>3.0.CO;2-H).
- [16] D.C. Walter, B. Lim, J. Schmidt, Realistic efficiency potential of next-generation industrial Czochralski-grown silicon solar cells after deactivation of the boron-oxygen-related defect center, *Prog. Photovoltaics Res. Appl.* 24 (7) (Jul. 2016) 920–928, <https://doi.org/10.1002/pip.2731>.
- [17] A. Cuevas, D. Macdonald, Measuring and interpreting the lifetime of silicon wafers, *Sol. Energy* 76 (1–3) (Jan. 2004) 255–262, <https://doi.org/10.1016/j.solener.2003.07.033>.
- [18] A. Richter, S.W. Glunz, F. Werner, J. Schmidt, A. Cuevas, Improved quantitative description of Auger recombination in crystalline silicon, *Phys. Rev. B* 86 (16) (Oct. 2012) 165202, <https://doi.org/10.1103/PhysRevB.86.165202>.
- [19] A. Schenck, Finite-temperature full random-phase approximation model of band gap narrowing for silicon device simulation, *J. Appl. Phys.* 84 (7) (1998) 3684–3695, <https://doi.org/10.1063/1.368545>.
- [20] T. Vogl, et al., Radiation tolerance of two-dimensional material-based devices for space applications, *Nat. Commun.* 10 (1) (Mar. 2019) 1202, <https://doi.org/10.1038/s41467-019-09219-5>.
- [21] M. Yamaguchi, et al., Deep level analysis of radiation-induced defects in Si crystals and solar cells, *J. Appl. Phys.* 86 (1) (1999) 217–223, <https://doi.org/10.1063/1.370698>.
- [22] A. Hamache, N. Sengouga, A. Meftah, M. Henini, Modeling the effect of 1 MeV electron irradiation on the performance of n+-p+ silicon space solar cells, *Radiat. Phys. Chem.* 123 (Jun) (2016) 103–108, <https://doi.org/10.1016/j.radphyschem.2016.02.025>.
- [23] J. Greulich, N. Wöhre, M. Glatthaar, S. Rein, Optical modeling of the rear surface roughness of passivated silicon solar cells, *Energy Proc.* 27 (2012) 234–239, <https://doi.org/10.1016/j.egypro.2012.07.057>.
- [24] B. Min, et al., A roadmap toward 24% efficient PERC solar cells in industrial mass production, *IEEE J. Photovoltaics* 7 (6) (Nov. 2017) 1541–1550, <https://doi.org/10.1109/JPHOT.2017.2749007>.
- [25] S. Mack, D. Herrmann, M. Lenes, M. Renes, A. Wolf, Progress in p-type tunnel oxide-passivated contact solar cells with screen-printed contacts, *Sol. RRL* 5 (5) (May 2021), <https://doi.org/10.1002/solr.202100152>.
- [26] G.P. Summers, E.A. Burke, M.A. Xapsos, Displacement damage analogs to ionizing radiation effects, *Radiat. Meas.* 24 (1) (Jan. 1995) 1–8, [https://doi.org/10.1016/1350-4487\(94\)00093-G](https://doi.org/10.1016/1350-4487(94)00093-G).
- [27] Standard: Qualification and quality requirements for space solar cells (AIAA S-111A-2014), in: *Standard: Qualification and Quality Requirements for Space Solar Cells (AIAA S-111A-2014)*, American Institute of Aeronautics and Astronautics, Inc., Washington, DC, 2014, <https://doi.org/10.2514/4.102806.001>.
- [28] M. Yamaguchi, S.J. Taylor, S. Matsuda, O. Kawasaki, Mechanism for the anomalous degradation of Si solar cells induced by high fluence 1 MeV electron irradiation, *Appl. Phys. Lett.* 68 (22) (May 1996) 3141–3143, <https://doi.org/10.1063/1.115804>.
- [29] A. Suzuki, High-efficiency silicon space solar cells, *Sol. Energy Mater. Sol. Cell.* 50 (1–4) (Jan. 1998) 289–303, [https://doi.org/10.1016/S0927-0248\(97\)00160-8](https://doi.org/10.1016/S0927-0248(97)00160-8).